Urea-Based Hydrothermally Derived Homogeneous Nanostructured $Ce_{1-x}Zr_xO_2$ ($x = 0-0.8$) Solid Solutions: A Strong Correlation between Oxygen Storage Capacity and Lattice Strain

Rui Si,[†] Ya-Wen Zhang,*,[†] Shi-Jie Li,[‡] Bing-Xiong Lin,[‡] and Chun-Hua Yan*,[†]

State Key Lab of Rare Earth Materials Chemistry and Applications & PKU-HKU Joint Lab on Rare Earth Materials and Bioinorganic Chemistry, Peking University, Beijing 100871, China, and College of Chemistry and Molecular Engineering, Peking University, Beijing 100871, China

$Ce_{1-x}Zr_xO_2$ ($x = 0-0.8$) nanoparticulate powders were prepared via a mild urea hydrolysis based hydrothermal method through homogeneous nucleation at 413 K followed by calcination at 773 or 1173 K. X-ray fluorescence (XRF) and energy-dispersive X-ray analysis (EDAX) measurements testify to the good stoichiometric homogeneity of Ce and Zr cations in the as-obtained $Ce_{1-x}Zr_xO_2$ products. X-ray photoelectron spectroscopy (XPS) and ultraviolet−visible (UV−vis) spectra exhibit that both surface and bulk ratios of Ce^{3+} to Ce^{4+} for the as-prepared $Ce_{1-x}Zr_xO_2$ nanocrystals increased with the zirconium content *x*. Powder X-ray diffraction (PXRD) patterns and Raman spectra demonstrate that the present $Ce_{1-x}Zr_xO_2$ samples were single-phase solid solutions with good structural homogeneity and high thermal stability up to 1273 K, and those with $x = 0.4-0.6$ retained a pseudocubic structure (*t″* phase) due to the small crystallite size effect. Transmission electron microscopy (TEM) micrographs reveal that the as-prepared CeO_2-ZrO_2 nanocrystals were highly crystallized with narrow size distribution. Nitrogen adsorption measurements show that the BET specific surface areas of the $Ce_{1-x}Zr_xO_2$ powders were improved by the incorporation of ZrO_2. The PXRD data and high-resolution TEM (HRTEM) images illuminate that the as-prepared and as-calcined $Ce_{1-x}Zr_xO_2$ ($x = 0.4-0.6$) powders kept a rather high strain level in the crystal lattice. The lattice strains in our $Ce_{1-x}Zr_xO_2$ catalysts show a linear relationship with their oxygen storage capacity (OSC) values. This linear correlation is explained on the basis of qualitative structural and defective analysis, and might find use in the screening and design of better-performing three-way catalysts (TWCs). The highest CO-OSC values of the studied CeO_2-ZrO_2 catalysts appeared for $Ce_{0.5}Zr_{0.5}O_2$ (543 μmol of CO g^{-1} at 773 K and 628 μmol of CO g^{-1} at 973 K).

Introduction

Ceria-based materials are of great significance and intensive interest for researchers because of their applications as diverse as ultraviolet (UV) absorbers, automotive three-way catalysts (TWCs), solid oxide fuel cells (SOFCs), and glass-polishing materials. For instance, pure or doped ceria exhibits strong absorption in the UV region and is hence used as a UV blocking material.[1] $CeO_2-Gd_2O_3$ and CeO_2-ZrO_2 materials have the potential to be applied in the next generation of compact SOFCs for their enhancement in oxygen-exchange processes and associated catalytic reactions.[2] Since 1995, CeO_2-ZrO_2 mixed oxides have gradually replaced pure CeO_2 as oxygen storage capacity (OSC) materials in the TWCs to reduce the emission of toxic pollutants (CO, NO$_x$, and hydrocarbons, etc.) from automobile exhaust, due to their enhanced reduction behavior and improved thermal stability at elevated temperatures.[3−5]

So far, numerous technical routes including ball milling,[6] coprecipitation,[7,8] sol−gel,[8,9] and hydrothermal synthesis[10] have been developed to prepare ceria and ceria−zirconia materials. For example, Hirano and Kato have investigated the hydrothermal synthesis of ceria in the presence of mild urea hydrolysis and obtained uniform CeO_2 nanoparticles.[11] Recently, Meeyoo

et al. synthesized nanostructured $Ce_{1-x}Zr_xO_2$ ($x = 0-1$) mixed oxides via urea hydrolysis based coprecipitation using $Ce(NO_3)_3$ as a starting material, and the as-derived CeO_2-ZrO_2 mixed oxides were somewhat nonhomogeneous in terms of microdomain or phase segregation.[12] To obtain the CeO_2-ZrO_2 mixed oxides with better textural stability and redox property, a number of research groups are devoting themselves to synthesizing the CeO_2-ZrO_2 solid solutions with high stoichiometric and structural homogeneity.[5,13]

In the latest decade, great effort has been devoted to investigating the complex compositions (stoichiometric and chemical homogeneity), crystal structure (phase purity and lattice defects), and textural properties (crystallite size, surface area, and thermal stability) of the CeO_2-ZrO_2 materials by various methods such as powder X-ray diffraction, Raman spectroscopy, transmission electron microscopy, X-ray photoelectron spectroscopy, and extended X-ray absorption fine structure (EXAFS). It has been agreed that the introduction of zirconia greatly enhances the surface areas, oxygen vacancies, thermal stability, and oxygen storage capacity of the ceria-based materials.[3−5,13−19] Recently, a direct correlation between the concentration of vacancy-interstitial oxygen defects and OSC has been validated in nanostructured ceria and ceria−zirconia systems.[17] However, the preparation and characterization of single-phase CeO_2-ZrO_2 materials with good structural homogeneity and high thermal stability were rarely reported.[6−8,13] For nanostructured CeO_2-ZrO_2 materials, both surface and bulk oxygen atoms could be

---

* Corresponding authors. Fax: +86-10-6275-4179. E-mail: chyan@chem.pku.edu.cn.
† State Key Lab of Rare Earth Materials Chemistry and Applications & PKU-HKU Joint Lab on Rare Earth Materials and Bioinorganic Chemistry.
‡ College of Chemistry and Molecular Engineering.

utilized in the redox process, whereas for bulk powders, only surface atoms.[4] As we know, some fundamental aspects (phase diagrams, the doping effects of zirconia, and the relationships between the textural stability, redox properties, and compositions) associated with the CeO_2-ZrO_2 solid solutions in the nanometric regime remain ambiguous.[4,5,13,19]

The targets of this work are to utilize a facile urea hydrolysis based hydrothermal method to synthesize nanostructured $Ce_{1-x}Zr_xO_2$ ($x = 0-0.8$) solid solutions with good structural homogeneity and high thermal stability, to investigate the surface chemistry, crystal structure, and textural properties of the as-obtained $Ce_{1-x}Zr_xO_2$ products, and further to uncover the doping effects of ZrO_2 into the ceria-based nanomaterials and the key factors determining the OSC values of the CeO_2-ZrO_2 catalysts. In this article, a strong correlation between oxygen storage capacity and lattice strain in the studied $Ce_{1-x}Zr_xO_2$ ($x = 0-0.8$) solid solutions has been forwarded, testified, and explained based on the qualitative analyses of their crystal structures and lattice defects. It is expected that this correlation can be applied to the estimation and design of better-performing CeO_2-ZrO_2 catalysts.

Experimental Section

1. Synthesis. To obtain $Ce_{1-x}Zr_xO_2$ ($x = 0-0.8$) solid solutions, quantitative solutions of $(NH_4)_2Ce(NO_3)_6$ (>99.0%, AR, Beijing Chem. Corp., China), $ZrO(NO_3)_2$ (AR, Beijing Liulidian Chemical Plant, China), and urea (>99.0%, AR, Beijing Chem. Corp., China) in the molar ratio of $Ce^{4+}:ZrO^{2+}$: urea = $(1 - x):x:15$ ($x = 0, 0.2, 0.4, 0.5, 0.6, 0.8$) were employed to prepare the stock solution of 80 mL with the cation concentration fixed at 0.1 mol L^{-1} in a Teflon bottle (inner volume: 100 mL), which was kept in a stainless steel autoclave. After the autoclave was sealed tightly, it was placed in a temperature-controlled electric oven and subjected to hydrothermal treatment at temperatures of 413 K for 24 h. After hydrothermal treatment, yellow precipitates were centrifugally separated, washed with deionized water and ethanol several times, and subsequently dried at 353 K in air overnight. The as-prepared $Ce_{1-x}Zr_xO_2$ powders were thus obtained with yields of ca. 90% and then calcined in still air at 773 or 1173 K for 4 h.

2. Characterization Methods. Elementary analysis was carried out on an Elementary Vario EL (Germany) system. X-ray fluorescence (XRF) data were obtained from a Bruker S4 Explorer spectrometer, using a power of 1 kW. Thermogravimetry (TG) analysis was performed with a Universal V2.60 TA instrument at a heating rate of 10 K min^{-1} from room temperature to 1273 K, using α-Al_2O_3 as a reference. Infrared spectra (IR) were obtained on a Nicolet Magna 750 FTIR spectrometer at a resolution of 4 cm^{-1} with a Nic-Plan IR microscope. Vis-Raman spectra were determined on a Renishaw (U.K.) spectrometer with an Ar ion laser of 514.5 nm excitation wavelength. Backscattering geometry was adopted for the measurement under the conditions of a laser power of 20 mW and a resolution of 4 cm^{-1}.

The powder X-ray diffraction (PXRD) patterns were recorded on a Rigaku D/MAX-2000 diffractometer with a slit of 0.5° at a scanning rate of 4 deg min^{-1}, using Cu Kα radiation ($\lambda = 1.5406$ Å). The lattice parameters were calculated with the software "LAPOD" of least-squares refinement of cell dimensions from powder data by Cohen's method.[20,21] The average grain size (D) was estimated according to the Scherrer equation,[22]

$$D = 0.90\lambda/\beta \cos\theta$$

where θ is the diffraction angle of the (1 1 1) peak of the cubic phase or the (1 0 1) peak of the tetragonal phase and β is the full width at half-maximum (fwhm) of the (1 1 1) or the (1 0 1) peak (in radian), which is calibrated from high purity silicon. The microstrain ϵ in the lattice (lattice strain) of the as-obtained nanocrystals was estimated by the single line method for analysis of X-ray diffraction line broadening, using a pseudo-Voigt profile function.[23] A slow scan rate of 1 deg min^{-1} in the range of 24-38° was carried out to ensure the quality of the PXRD data for calculating grain size and microstrain. The BET specific surface area (S) was measured by nitrogen adsorption at 78.3 K, using an ASAP 2010 analyzer (Micromeritics Co. Ltd.), after outgassing the sample at 423 K for at least 4 h under vacuum, down to a residual pressure better than 10 μm Hg. Surface composition was determined by X-ray photoelectron spectroscopy (XPS) in an ion-pumped chamber (evacuated to 1.3×10^{-8} Torr) of an Axis Ultra (U.K.) spectrometer equipped with a focused monochromatized X-ray source (Al Kα, $h\nu = 1486.6$ eV) at a power of 225 W. A hemispherical analyzer collected the photoelectrons at an angle of 90° from the surface. The binding energy (BE) for the samples was calibrated by setting the measured BE of C 1s to 284.6 eV. To avoid the reduction of Ce^{4+} to Ce^{3+} by the irradiation damage of the X-ray beam on the tested samples, the collection time was set as less than 10 min for each measurement. Microdomain stoichiometry of the as-prepared nanocrystals was determined by energy-dispersive X-ray analysis (EDAX) at a resolution of 159 eV (200CX, JEOL). The spatial resolution of the EDAX measurements is 20 nm under the STEM mode and the statistic error of the EDAX system used is about 5-10%. Transmission electron microscopy (TEM) and high-resolution TEM (HRTEM) characterization were performed with a Philips Tecnai F30 FEG-TEM operated at 300 kV. The samples were supported on carbon-coated copper grids by dropping the ethanol suspension containing uniformly dispersed oxide powders. The as-washed $Ce_{1-x}Zr_xO_2$ products were dispersed in ethanol at a concentration of ca. 10^{-3} mol L^{-1} before drying, and then sonicated at room temperature to obtain a transparent colloidal solution. The UV-vis absorbance spectra of the above solutions were recorded on a Hitachi U-3010 spectrometer with use of a quartz cell (10 mm path length) and pure ethanol was used as a blank. The optical absorption coefficient α was calculated according to the following equation:

$$\alpha = [(2.303 \times 10^3)A\rho]/lc$$

where A is the absorbance of a sample, ρ is the real density of $Ce_{1-x}Zr_xO_2$, l is the path length, and c is the concentration of $Ce_{1-x}Zr_xO_2$ suspensions.

By pulse technique,[24] the oxygen storage capacity (OSC) experiments were performed with a GC-7890T gas chromatograph (Shanghai Tianmei Instrument Co. Ltd., China) as the analytical device. The samples were oxidized at a given temperature in flowing O_2 (5.29%)/He injected (2 mL) periodically five times at intervals of 2 min, and then reduced at the same temperature with pulses of 5 mL of CO (5.0%)/He. The CO-OSC values were determined by the amount of CO consumed during the CO pulse. Each measurement was repeated five times and the results were averaged.

Results and Discussion

1. Elementary Composition and Chemical Valence. The bulk and microdomain metal compositions in the as-prepared products were determined by XRF and EDAX measurements,
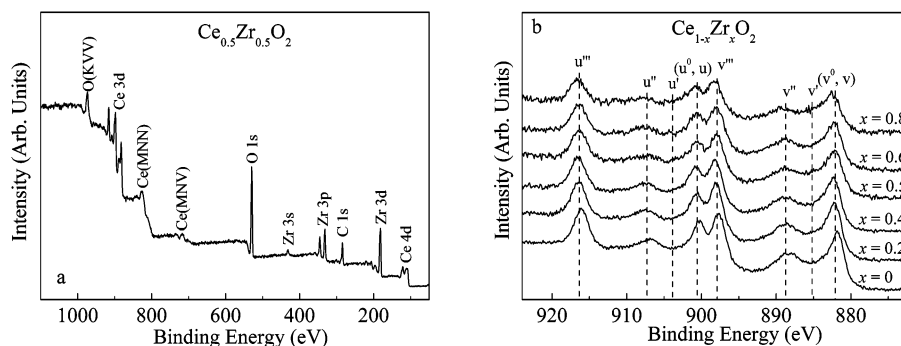
Ce$_{1-x}$Zr$_x$O$_2$ ($x = 0-0.8$) Solid Solutions

J. Phys. Chem. B, Vol. 108, No. 33, 2004 **12483**

Figure 1. XPS spectra of the as-prepared Ce$_{1-x}$Zr$_x$O$_2$ samples: (a) wide spectrum ($x = 0.5$) and (b) Ce 3d spectra ($x = 0-0.8$).

TABLE 1: Practical Compositions of the As-Prepared Ce$_{1-x}$Zr$_x$O$_2$ ($x = 0.2-0.8$) Samples Determined by XRF and EDAX Measurements

	$x =$				
	0.2	0.4	0.5	0.6	0.8
Zr (mol %) from XRF	21	39	51	57	78
Zr (atom %) from EDAX	22	39	53	57	81

TABLE 2: Phases, Space Groups, and Lattice Parameters (a or c) of the Ce$_{1-x}$Zr$_x$O$_2$ ($x = 0-0.8$) Solid Solutions Calcined at 1173 K

x	phase	space group	lattice parameter (Å)
0	cubic	$Fm3m$	$a = 5.4173(1)$
0.2	t''	$P4_2/nmc$	$a = 5.3637(1)$
0.4	t''	$P4_2/nmc$	$a = 5.3201(2)$
0.5	t''	$P4_2/nmc$	$a = 5.2842(3)$
0.6	t''	$P4_2/nmc$	$a = 5.2461(4)$
0.8	t	$P4_2/nmc$	$a = 5.1518(6), c = 5.2336(9)$

respectively. Table 1 exhibits that the experimental Zr content x from either XRF or EDAX was in good agreement with the target composition within the limit of each detection, indicating the good stoichiometric homogeneity of Ce and Zr cations in the as-prepared Ce$_{1-x}$Zr$_x$O$_2$ ($x = 0.2-0.8$) products.

By elementary and FTIR analyses (see Table 1S and Figure 1S), we found that the as-prepared Ce$_{1-x}$Zr$_x$O$_2$ samples contained a portion of impurities including some adsorbed solvents (water and ethanol) and a small amount of NO$_3^-$ ions. The impure species in the as-prepared Ce$_{1-x}$Zr$_x$O$_2$ products could be eliminated by calcination in air below 773 K and the total weight loss of each sample was between 5.6 and 12.8% (see TG results in Table 1S).

The elementary composition and chemical valence on the surface of the as-prepared Ce$_{1-x}$Zr$_x$O$_2$ particulate powders were detected by XPS. Figure 1a typically depicts the XPS survey spectrum of the sample Ce$_{0.5}$Zr$_{0.5}$O$_2$. Core levels of Ce 3d, Ce 4d, Zr 3s, Zr 3p, Zr 3d, C 1s, and O 1s can be identified. All the spectral features were fitted with Gaussian distributions and the determined peak positions of Ce 3d$_{5/2}$, Ce 3d$_{3/2}$, Zr 3d$_{5/2}$, Zr 3d$_{3/2}$, and O 1s are listed in Table 2S.

The complex spectrum of Ce 3d can be decomposed into eight components with the assignment defined in Figure 1b. According to the previous research,[25] for CeO$_2$-ZrO$_2$ mixed oxides, the bands v' and u' are the satellites arising from the Ce 3d$_{5/2}$ and Ce 3d$_{3/2}$ ionizations of Ce^{3+}. From Figure 1b, it can be seen that the chemical valence of cerium on the surface of our Ce$_{1-x}$Zr$_x$O$_2$ sample was mainly Ce^{4+} plus a small fraction of Ce^{3+}. The relative intensities of v' and u' to the other six bands increased with the accreted zirconium content x, revealing that the surface ratio of Ce^{3+} to Ce^{4+} on the as-prepared Ce$_{1-x}$Zr$_x$O$_2$ powder was enhanced by the incorporation of zirconia.
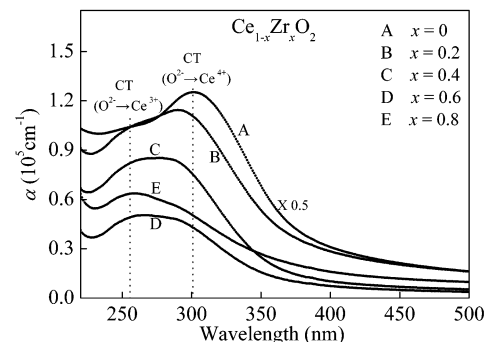

Figure 2. UV−vis absorption spectra of the as-washed Ce$_{1-x}$Zr$_x$O$_2$ ($x = 0-0.8$) nanocrystals dispersed in ethanol.

Figure 2 is the UV−vis absorption spectra of the as-washed Ce$_{1-x}$Zr$_x$O$_2$ ($x = 0-0.8$) samples. It was reported that polycrystalline ceria has strong absorption in the UV region with the absorption threshold near 400 nm[26] and polycrystalline tetragonal zirconia has a UV absorption threshold near 240 nm.[27] The UV−vis absorption spectra of our Ce$_{1-x}$Zr$_x$O$_2$ nanocrystals dispersed in ethanol have two bands at ca. 300 and 260 nm wavelength. The absolute absorbance coefficient α in the above wavelength range was generally in proportion to the cerium content $1 - x$. Thus, the above two bands at ca. 300 and 260 nm wavelength can be attributed to the O^{2-} → Ce^{4+} and O^{2-} → Ce^{3+} charge transfer (CT) transitions, respectively.[27] From Figure 2, it is noted that the absorption ratio of CT (O^{2-} → Ce^{3+}) to CT (O^{2-} → Ce^{4+}) increased with x, suggesting that the bulk ratio of Ce^{3+} to Ce^{4+} in our Ce$_{1-x}$Zr$_x$O$_2$ powder was also enhanced by the doping of ZrO$_2$. The enhancement of both surface and bulk ratios of Ce^{3+} to Ce^{4+} is probably because the insertion of the smaller Zr^{4+} ion ($r_{VIII} = 0.84$ Å) can partly compensate for the expansion of the crystal lattice, which originates from the transformation of the Ce^{4+} ion ($r_{VIII} = 0.97$ Å) to the larger Ce^{3+} ion ($r_{VIII} = 1.10$ Å).[14]

2. Crystal Structure and Thermal Stability. In previous research, it has been observed that the CeO$_2$−ZrO$_2$ mixed oxides have a quite complex phase diagram, containing three stable phases (monoclinic, tetragonal (t), and cubic) and two metastable phases (t', t'').[28−31] Among the above three tetragonal phases (t, t', and t''), the t phase is formed through a diffused phase decomposition, while the t' phase is obtained through a diffusionless transition, and the t'' phase is an intermediate phase between t' and cubic CeO$_2$ and very close to the fluorite cubic structure except that there exists the displacement of the oxygen atom in its crystal lattice.[28−31]

Figure 3a shows the PXRD patterns of the as-prepared Ce$_{1-x}$Zr$_x$O$_2$ ($x = 0-0.8$) powders. The broadening of the reflections in the diffractograms distinctly indicates their nanocrystalline nature and thus makes it difficult to explore the
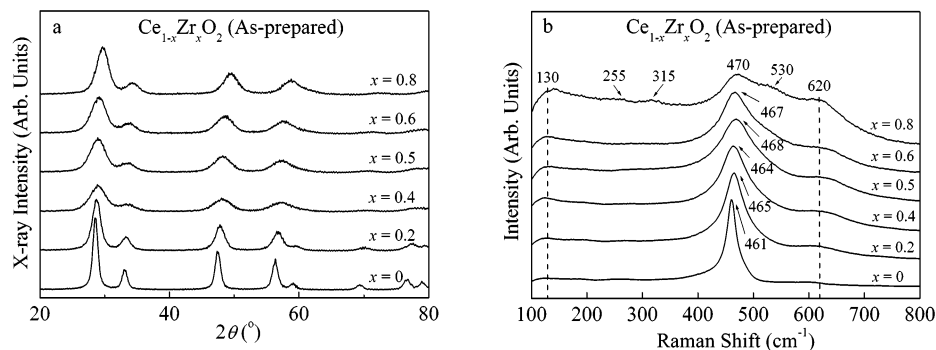
Figure 3. PXRD patterns (a) and Raman spectra (b) of the as-prepared $Ce_{1-x}Zr_xO_2$ ($x = 0-0.8$) samples.

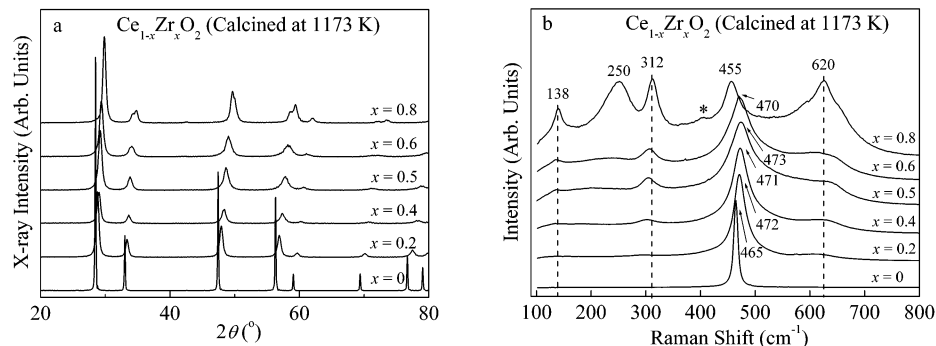**Figure 4.** PXRD patterns (a) and Raman spectra (b) of the $Ce_{1-x}Zr_xO_2$ ($x = 0-0.8$) samples calcined at 1173 K. The asterisk (∗) indicates fluorescence.

crystal structure of the present samples. Therefore, we utilized Raman spectroscopy, an effective tool for detecting the crystal structure of fine particles, to determine the exact phases of our CeO_2-ZrO_2 samples. Figure 3b is the Vis−Raman spectra of the as-prepared $Ce_{1-x}Zr_xO_2$ powders. For $Ce_{0.2}Zr_{0.8}O_2$ ($x = 0.8$), three Raman peaks at 130, 470, and 620 cm^{-1} and three weak bands at ca. 255, 315, and 530 cm^{-1}, originating from the six Raman active modes ($A_{1g} + 2B_{1g} + 3E_g$) of t-ZrO_2, could be located.[32] While for $x = 0-0.6$, the $Ce_{1-x}Zr_xO_2$ samples showed one strong Raman peak at 461−468 cm^{-1} (F_{2g} mode of cubic CeO_2) and two weak bands at ca. 130 and 620 cm^{-1}, attributed to the presence of defective structure in CeO_2-ZrO_2 materials.[30]

Figure 4 shows the PXRD patterns and Raman spectra of the $Ce_{1-x}Zr_xO_2$ samples calcined at 1173 K. After high-temperature calcination, the powders gave stronger, better-defined PXRD and Raman peaks. The symmetric peaks in Figure 4a obviously exhibit the single-phase nature of the as-calcined $Ce_{1-x}Zr_xO_2$ ($x = 0-0.8$) powders. The as-calcined CeO_2 and $Ce_{0.2}Zr_{0.8}O_2$ samples maintained cubic and stable tetragonal (t) structures, respectively, determined from Raman spectra (see Figure 4b). The disappearance of the weak bands at ca. 135 and 620 cm^{-1} for pure CeO_2 suggested the absence of defective structure in its crystal lattice after the sintering process. For $x = 0.2-0.6$, the as-calcined $Ce_{1-x}Zr_xO_2$ powders showed a metastable phase (t''), based on their Raman bands lying at ca. 138, 312, 470−473, and 620 cm^{-1}.[30] Table 2 shows the determined phases, space groups, and lattice parameters of the $Ce_{1-x}Zr_xO_2$ samples calcined at 1173 K. Pure CeO_2 is of fluorite cubic structure with lattice parameter $a = 5.4173$ Å (JCPDS card no. 34-394) and $Ce_{0.2}Zr_{0.8}O_2$ is of a stable tetragonal (t) phase with the lattice parameters of $a = 5.1518$ Å and $c = 5.2336$ Å, close to those of the polycrystalline $Ce_{0.2}Zr_{0.8}O_2$ sample reported by Kašpar et al. with the Rietveld refinement method ($a = 5.1516$ Å, $c = 5.2405$ Å).[33] When $x = 0.2-0.6$, the $Ce_{1-x}Zr_xO_2$ samples showed a metastable t'' structure with lattice parameters of 5.2461−5.3637 Å. Figure 5 displays the nearly linear relationship between the cubic root

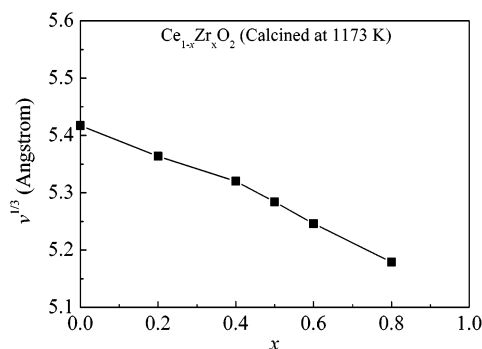**Figure 5.** Cubic root of the lattice volume ($V^{1/3}$) of the $Ce_{1-x}Zr_xO_2$ ($x = 0-0.8$) samples calcined at 1173 K as a function of zirconia content x.

of lattice volume ($V^{1/3}$) and the zirconium content x of the $Ce_{1-x}Zr_xO_2$ sample. According to Vegard's law, the studied CeO_2-ZrO_2 materials can be assigned to solid solutions, not mixed oxides. It reveals that the smaller Zr^{4+} ion ($r_{VIII} = 0.84$ Å) can substitute the position of Ce^{4+} ion ($r_{VIII} = 0.97$ Å) in the whole doping range of $x = 0.2-0.8$ by the present synthetic method.

Further investigation on the structural homogeneity and thermal stability of $Ce_{1-x}Zr_xO_2$ ($x = 0-0.8$) materials was carried out by following the criterion suggested by Kašpar et al.[34] No asymmetric peaks were found in the PXRD patterns (Figure 2S) of CeO_2-ZrO_2 samples calcined at 1273 K, indicating that the $Ce_{1-x}Zr_xO_2$ powders were single-phase solid solutions, even after calcination at 1273 K. Raman spectra show that the $Ce_{1-x}Zr_xO_2$ samples calcined at 1273 K preserved the same phases as those calcined at 1173 K, except for a phase transformation from t'' to t' for $Ce_{0.4}Zr_{0.6}O_2$ that was determined by the peaks at ca. 139, 247, 312, 475, and 620 cm^{-1} after calcination (see Figure 2S).[3] Therefore, our $Ce_{1-x}Zr_xO_2$ ($x = 0-0.8$) solid solutions possessed good structural homogeneity and high thermal stability up to 1273 K.

Ce$_{1-x}$Zr$_x$O$_2$ ($x = 0-0.8$) Solid Solutions

J. Phys. Chem. B, Vol. 108, No. 33, 2004 **12485**

TABLE 3: Particle Sizes (D) and BET Specific Surface Areas (S) of the Ce$_{1-x}$Zr$_x$O$_2$ ($x = 0-0.8$) Samples

	$x =$					
	0	0.2	0.4	0.5	0.6	0.8
D (nm)						
as-prepared	5.2[a] ± 0.9[b]	4.2 ± 0.7	4.2 ± 0.5	5.0 ± 0.7	3.9 ± 0.5	4.3±0.6
	(10)[c]	(5.6)	(2.9)	(3.0)	(3.1)	(3.8)
calcined at 773 K	6.5 ± 1.2	5.0 ± 0.7	5.0 ± 0.7	7.4 ± 1.3	5.6 ± 0.9	6.2 ± 1.0
	(11)	(6.4)	(3.9)	(3.7)	(4.3)	(5.5)
calcined at 1173 K	48 ± 29	33 ± 5	14 ± 4	21 ± 7	19 ± 3	21 ± 4
	(−)	(18)	(15)	(14)	(13)	(17)
S (m^2 g^{-1})						
as-prepared	97	151	219	172	226	210
calcined at 773 K	76	101	100	104	89	76
calcined at 1173 K	7	26	35	34	34	38

[a] Calculated from TEM. [b] The standard deviation of a. [c] Calculated from XRD by the Scherrer equation.

Different from the bulk Ce$_{1-x}$Zr$_x$O$_2$ ($x = 0.3-0.65$) materials which exhibit the t' phase at room temperature in previous report,[28] our Ce$_{1-x}$Zr$_x$O$_2$ ($x = 0.4-0.6$) solid solutions showed a t'' structure at ambient conditions. The stabilization of a higher symmetric structure, t'' phase in our work, is believed to be caused by the small crystallite size effect, i.e. the contribution of surface, interfacial, and strain energies of the crystalline.[35] For the ZrO$_2$-based system, this size effect has been previously investigated and demonstrated by a number of research groups, and it normally occurred at a critical size between 10 and 300 nm.[35-38] Recently, Conesa's group observed that the Ce$_{0.5}$Zr$_{0.5}$O$_2$ nanoparticles (ca. 5 nm) prepared by the microemulsion method possessed the t'' phase, instead of the t' phase.[39] The crystallite size in our case is 14−21 nm (see Table 3) for the Ce$_{1-x}$Zr$_x$O$_2$ ($x = 0.4-0.6$) nanocrystals that preferred a pseudocubic t'' structure.

3. Formation of Homogeneous Ce$_{1-x}$Zr$_x$O$_2$ ($x = 0-0.8$) Solid Solutions. A lot of researchers have focused on preparing single-phase CeO$_2$−ZrO$_2$ solid solutions due to their better textural property, thermal stability, and redox behaviors compared to microdomain- or phase-segregated nonhomogeneous ones.[13] Previously, Meeyoo et al. synthesized nanostructured Ce$_{1-x}$Zr$_x$O$_2$ ($x = 0-1$) mixed oxides via urea hydrolysis-based coprecipitation using Ce(NO$_3$)$_3$ as a starting material, while the as-derived products with $x \geq 0.5$ appeared somewhat phase segregated upon calcination at 773 K.[12] As shown in the former parts, present CeO$_2$−ZrO$_2$ nanomaterials are truly solid solutions with good structural homogeneity and high thermal stability up to 1273 K. There is an important question for us to solve: What are the key factors that led to the formation of our homogeneous CeO$_2$−ZrO$_2$ solid solutions?

It is well-known that temperature-dependent urea hydrolysis is a mild process to produce base species (OH$^-$), with which metal ions can precipitate via homogeneous nucleation under controlled pH values.[40] In this work, ZrO^{2+} and Ce^{4+} ions might simultaneously hydrolyze into the polynuclear species such as [Ce(OH)$_m$(H$_2$O)$_n$]$^{4-m}$ and [Zr(OH)$_p$(H$_2$O)$_q$]$^{4-p}$ ($m + n$ and $p + q$ denoting the coordination numbers of the metal ions),[41,42] respectively, due to the nearly same solubility product values of Ce(OH)$_4$ (pK_{sp} = 47.7) and Zr(OH)$_4$ (pK_{sp} = 48.2). Promptly, these polynuclear species were co-mingled homogeneously and transformed to hydrated (Ce,Zr)-hydroxides ([(Ce$_{1-x}$Zr$_x$)(OH)$_y$(H$_2$O)$_z$]$^{4-y}$), where $y + z$ is the coordination number of cations. The highly homogeneous co-mixture during the formation of hydrated (Ce,Zr)-hydroxides must be the crucial factor to achieve CeO$_2$−ZrO$_2$ solid solutions with good stoichiometric homogeneity. By the hydrothermal aging process, the (Ce,Zr)-hydroxides could be transferred to the CeO$_2$−ZrO$_2$ nanocrystals via dissolution and recrystallization under ap-

propriate experimental conditions. The as-obtained crystallites had better resistance to phase segregation induced by the heat-induced mass diffusion than amorphous matter during the sintering process.

4. Texture and Lattice Strain. Figure 6 shows the typical TEM micrographs of the as-prepared Ce$_{1-x}$Zr$_x$O$_2$ nanocrystals. The lattice fringes with the interplanar spacing of 0.33, 0.31, and 0.29 nm in Figures 6a−c were determined to be associated with the {1 1 1} facets of Ce$_{0.8}$Zr$_{0.2}$O$_2$ (Figure 6a), {1 1 1} facets of Ce$_{0.5}$Zr$_{0.5}$O$_2$ (Figure 6b), and {1 0 1} facets of Ce$_{0.2}$Zr$_{0.8}$O$_2$ (Figure 6c), respectively, suggesting that the CeO$_2$−ZrO$_2$ products were well crystallized after hydrothermal treatment. The as-prepared powders were composed by uniform nanoparticles with narrow size distribution and the average particle sizes were 4.2 ± 0.7, 5.0 ± 0.7, and 4.3 ± 0.6 nm for Ce$_{0.8}$Zr$_{0.2}$O$_2$, Ce$_{0.5}$Zr$_{0.5}$O$_2$, and Ce$_{0.2}$Zr$_{0.8}$O$_2$, respectively (see Figure 6d−f).

The particle sizes D from both XRD and TEM for the Ce$_{1-x}$Zr$_x$O$_2$ ($x = 0-0.8$) powders are listed in Table 3. The difference between these two sizes was clearly observed and the reason lies in that the contribution of lattice strain on the broadening of the XRD peaks causes the Scherrer equation to be partially invalidated under this condition. The slight mismatch of lattice fringes in the TEM micrographs (Figure 6a−c) directly exhibits the existence of high microstrains in the Ce$_{1-x}$Zr$_x$O$_2$ crystal lattices after hydrothermal processing.[43,44] Therefore, we define the TEM size as the particle size and the D value of the Ce$_{1-x}$Zr$_x$O$_2$ powders decreased with the doping of ZrO$_2$ after calcination at 1173 K (see Table 3).

Table 3 also lists the BET specific surface areas S of the Ce$_{1-x}$Zr$_x$O$_2$ ($x = 0-0.8$) powders. The largest surface area among the as-prepared samples is 226 m^2 g^{-1} for Ce$_{0.4}$Zr$_{0.6}$O$_2$ ($x = 0.6$), higher than that of the CeO$_2$−ZrO$_2$ materials prepared by hydrothermal synthesis (104−184 m^2 g^{-1}).[10] After calcining at 773 K, S values of the Ce$_{1-x}$Zr$_x$O$_2$ solid solutions were in the range 76−104 m^2 g^{-1}, close to that of the reported CeO$_2$−ZrO$_2$ catalysts (80−110 m^2 g^{-1}) prepared by the coprecipitation method with ammonia.[45] Further calcined at 1173 K, the doped Ce$_{1-x}$Zr$_x$O$_2$ ($x = 0.2-0.8$) powders showed a surface area between 26 and 38 m^2 g^{-1}. The introduction of ZrO$_2$ to CeO$_2$ markedly improved the surface areas of both as-prepared and as-calcined samples, possibly due to the inhibition of grain growth and fusion of the as-prepared nanocrystals during the high-temperature sintering process.[46] Figure 7 displays the calculated microstrain in the crystal lattice of the CeO$_2$−ZrO$_2$ solid solutions as a function of zirconia content x at different heat-treating temperatures. The high lattice strain in the as-prepared sample (1.0−5.6%) was eliminated partly after calcination (773 K, 0.8−3.3%; 1173 K, 0.18−0.58%). At a fixed heat-treating temperature (413, 773, or 1173 K), the max lattice
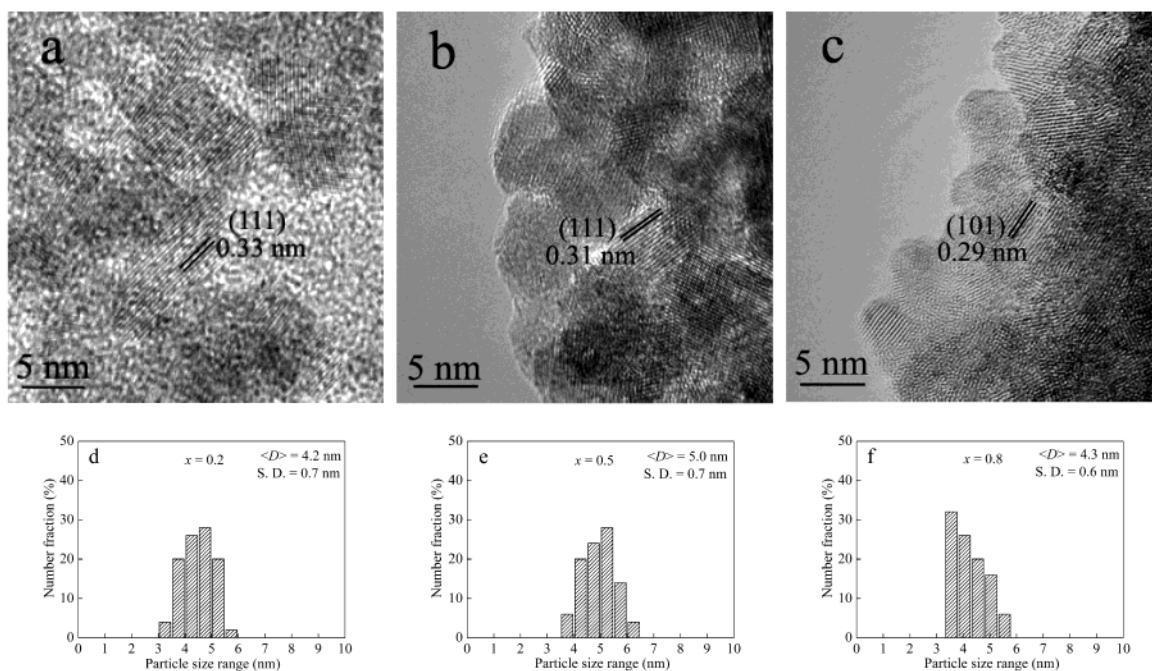
Figure 6. TEM micrographs of the as-prepared $Ce_{1-x}Zr_xO_2$ samples: (a) $x = 0.2$; (b) $x = 0.5$; (c) $x = 0.8$; (d−f) the size distribution histograms of panels a−c.

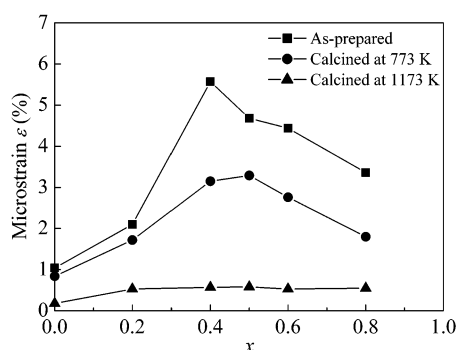**Figure 7.** Microstrain in the lattice of the $Ce_{1-x}Zr_xO_2$ ($x = 0-0.8$) solid solutions as a function of Zr content x.

strain appeared in the medium doping range of $x = 0.4-0.6$. Typical HRTEM images were magnified in Figure 8 to confirm the different strain levels in the $Ce_{1-x}Zr_xO_2$ system.[43,44] It is obvious that the lattice fringes of {1 1 1} facets on the crystallite of pure ceria (Figure 8a,c) are clearer and straighter than those on the crystallite of zirconia-doped ceria ($Ce_{0.5}Zr_{0.5}O_2$, Figure 8b,d), revealing the doping effect of ZrO_2 on the stabilization of the high strain level in the CeO_2-ZrO_2 system at the various sintering temperatures (773 and 1173 K).

It is well-known that lattice strain is a kind of metrology displaying the distorted degree in a real crystalline, compared to the perfect structural model. For the CeO_2-ZrO_2 system, lattice strain in the as-calcined crystalline is considered to originate from the following three ways:

(a) The nonhomogeneous distribution of Ce and Zr cations in the $Ce_{1-x}Zr_xO_2$ structure due to the substitution reaction of Ce^{4+} ion by Zr^{4+} ion. This reaction can be written in Kroger and Vink notations as:

$$ZrO_2 \leftrightarrow Zr_{Ce}^{\times} + 2O_O^{\times} \qquad (1)$$
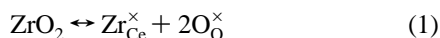
where $Zr_{Ce}^{\times}$ represents a Zr^{4+} occupying the site normally occupied by a Ce^{4+}, and $O_o^{\times}$ is the oxygen atom.

(b) The creation of pure oxygen vacancy as well as Ce^{3+} ion, which could be enhanced by the incorporation of ZrO_2.[14]

$$2Ce_{Ce}^{\times} + O_O^{\times} \leftrightarrow 2Ce_{Ce}' + V_O^{\bullet\bullet} + {}^1\!/_2O_2 \qquad (2)$$
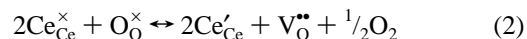
where Ce_{Ce}' is a Ce^{3+} occupying the site normally occupied by a Ce^{4+} due to the transformation from Ce^{4+} to Ce^{3+}, and $V_O^{\bullet\bullet}$ repesents the O^{2-} vacancy produced by the release of O_2.

(c) The Frenkel-type vacancy−interstitial oxygen defects produced by the displacement of oxygen atom from tetrahedral to octahedral sites in the $Ce_{1-x}Zr_xO_2$ crystal lattice:

$$O_O^{\times} \leftrightarrow V_O^{\bullet\bullet} + O_i'' \qquad (3)$$
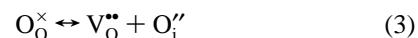
where O_i'' is the oxygen ion in interstitial position. Mamontov et al. discovered that doping of ZrO_2 into pure CeO_2 could stabilize this type of defect, especially after high-temperature calcination.[17]

Since our $Ce_{1-x}Zr_xO_2$ ($x = 0-0.8$) solid solutions were demonstrated to have good stoichiometric and structural homogeneity, the contribution of nonhomogeneous cation substitution on lattice strain should be neglected in this work. We think that the high lattice strain level in our CeO_2-ZrO_2 solid solutions is related to the large density of oxygen defects including pure oxygen vacancy and vacancy−interstitial oxygen defects in the crystal lattices.

The samples with relatively high lattice strain level appeared when $x = 0.4-0.6$ for $Ce_{1-x}Zr_xO_2$ (see Figure 7) so that the density of oxygen defects was also large in their crystal structures. This may be caused by the defective pseudocubic t'' structure of $Ce_{1-x}Zr_xO_2$ ($x = 0.2-0.6$), which contains more oxygen defects than the fluorite cubic structure of pure CeO_2.[29] When the zirconium content x is further raised to 0.8, a nondefective t phase forms and the density of oxygen defects sharply reduces, comparing to the defective t'' structure.[29,47,48] This leads to the lower lattice strain for $Ce_{0.2}Zr_{0.8}O_2$. Therefore, the zirconium content x influences not only the crystal structure, but also the concentration of oxygen defects and thus-resulted lattice strain in the $Ce_{1-x}Zr_xO_2$ ($x = 0-0.8$) solid solutions.

Ce$_{1-x}$Zr$_x$O$_2$ ($x = 0-0.8$) Solid Solutions

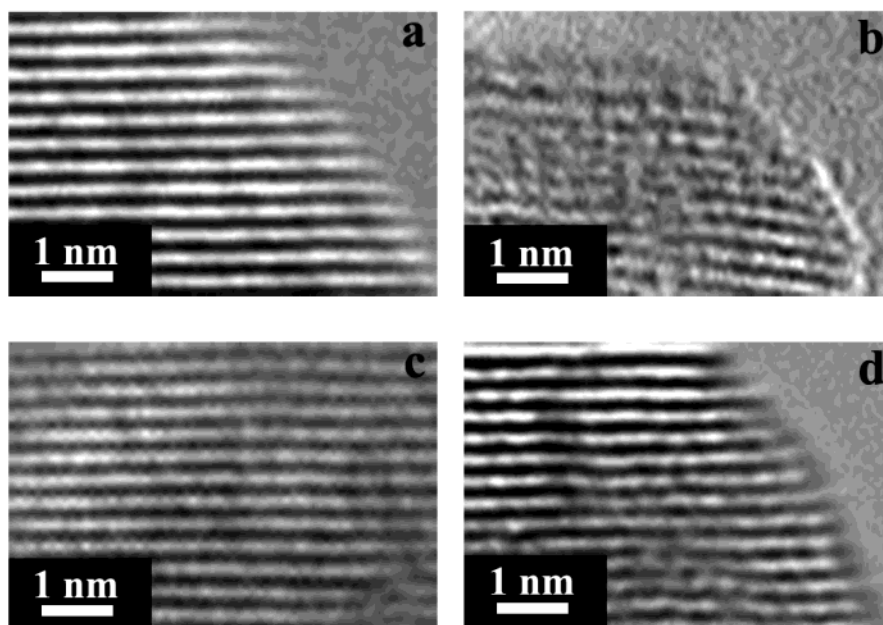*J. Phys. Chem. B, Vol. 108, No. 33, 2004* **12487**

Figure 8. HRTEM images of the Ce$_{1-x}$Zr$_x$O$_2$ samples: (a) $x = 0$, calcined at 773 K; (b) $x = 0.5$, calcined at 773 K; (c) $x = 0$, calcined at 1173 K; (d) $x = 0.5$, calcined at 1173 K.

TABLE 4: CO-OSC Values of the Ce$_{1-x}$Zr$_x$O$_2$ ($x = 0-0.8$) Catalysts

		$x =$					
		0	0.2	0.4	0.5	0.6	0.8
OSC (μmol CO g^{-1})	**C5**^{a}	239	353	505	543	486	304
	C9^b	64	484	607	628	574	398

^{a} Calcined at 773 K and measured at 773 K. ^{b} Calcined at 1173 K and measured at 973 K.

5. OSC Value and Its Correlation with Lattice Strain. The Ce$_{1-x}$Zr$_x$O$_2$ ($x = 0-0.8$) powders calcined at 773 and 1173 K were selected as the catalysts for the OSC measurements on CO conversion:

$$CO + {}^1\!/_2 O_2 \rightarrow CO_2$$
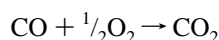
For convenience, we denote the Ce$_{1-x}$Zr$_x$O$_2$ catalysts calcined at 773 K and tested at 773 K as **C5**, and those calcined at 1173 K and tested at 973 K as **C9**. The CO-OSC values of the tested catalysts are listed in Table 4 and their order is as follows: Ce$_{0.5}$Zr$_{0.5}$O$_2$ > Ce$_{0.6}$Zr$_{0.4}$O$_2$ > Ce$_{0.4}$Zr$_{0.6}$O$_2$ > Ce$_{0.8}$Zr$_{0.2}$O$_2$ > Ce$_{0.2}$Zr$_{0.8}$O$_2$ > CeO$_2$ for both **C5** and **C9** series. The highest OSC value of our CeO$_2$–ZrO$_2$ solid solutions appeared for Ce$_{0.5}$Zr$_{0.5}$O$_2$—543 μmol of CO g^{-1} at 773 K and 628 μmol of CO g^{-1} at 973 K, which are comparable with the report by Descorme et al. (540 μmol of CO g^{-1} at 673 K for Ce$_{0.5}$Zr$_{0.5}$O$_2$).[16]

It has been found that there is a weak relationship between the particle sizes D or surface area S and the OSC values of **C5** or **C9** (see Table 3 and Figure 3S), indicating that the external texture is not the key factor governing the OSC performance of the present Ce$_{1-x}$Zr$_x$O$_2$ solid solutions. According to former discussions, lattice strain can reflect the density of oxygen defects—the active oxygen sites for storing and releasing oxygen—and thus we supposed that there must be some connection between the lattice strain and oxygen storage capacity for the studied CeO$_2$–ZrO$_2$ catalysts. Figure 9 shows the plots of the OSC values for **C5** and **C9** as a function of microstrain ϵ in the Ce$_{1-x}$Zr$_x$O$_2$ crystal lattice. A very good linear correlation can be determined and the OSC values of our
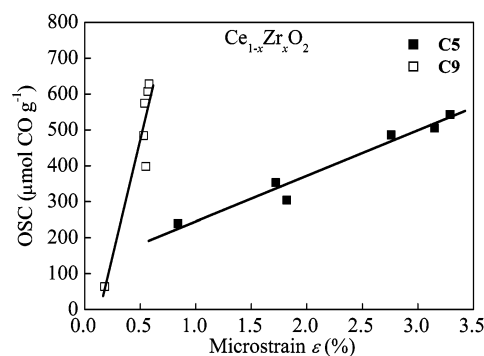

Figure 9. CO-OSC values of the Ce$_{1-x}$Zr$_x$O$_2$ ($x = 0-0.8$) catalysts as a function of the microstrain ϵ in the crystal lattice.

Ce$_{1-x}$Zr$_x$O$_2$ catalysts were in proportion to their lattice strain as expected. Furthermore, the slope for the **C9** series is remarkably larger than that for **C5**, revealing stronger dependence of the OSC value on lattice strain for the CeO$_2$–ZrO$_2$ catalysts during the high-temperature measurements than the low-temperature measurements.

The importance of the above correlation lies in the following two points: (1) the oxygen storage capacity of as-prepared CeO$_2$–ZrO$_2$ catalysts may be evaluated according to the lattice strain obtained by the simple analysis of the PXRD data, considering that the routine OSC measurement is a prolonging work; and (2) better-performing CeO$_2$–ZrO$_2$ catalysts can be designed by starting from the internal structure point, i.e., how to enhance the lattice strain in the CeO$_2$–ZrO$_2$ solid solutions. Through this research, we expect that further aliovalent doping (such as trivalent rare earth ions, bivalent Ca^{2+}, Mg^{2+} and so on) in the CeO$_2$–ZrO$_2$ binary system would improve its oxygen storage capacity because of both the predicated introduction of more oxygen vacancies and the stabilization of the pseudocubic t'' structure, which promises further research.

Conclusions

By elaborately selecting experimental parameters such as the starting metal salts and crystallizing route, we achieved nanostructured Ce$_{1-x}$Zr$_x$O$_2$ ($x = 0-0.8$) solid solutions via a facile

urea hydrolysis-based hydrothermal method. The as-obtained CeO_2-ZrO_2 products were single-phase solid solutions with good structural homogeneity and high thermal stability up to 1273 K. By multiple characterizations, the doping effects of ZrO_2 into pure CeO_2 were investigated and demonstrated as follows: (a) enhancing the surface and bulk ratios of Ce^{3+} to Ce^{4+}; (b) stabilizing the surface areas, particularly during the sintering process; and (c) improving the OSC values. It was observed that the $Ce_{1-x}Zr_xO_2$ ($x = 0.4-0.6$) powders preferred a metastable t'' phase to the reported t' phase, as the result of small crystallite size effect. The stabilization of pseudocubic t'' structure leads to the high strain level in the $Ce_{1-x}Zr_xO_2$ ($x = 0.4-0.6$) crystal lattice. Furthermore, a linear relationship between the lattice strain and the OSC value of the CeO_2-ZrO_2 catalyst has been validated. This correlation can be used as a tool to evaluate the oxygen storage capacity by the analysis of the powder X-ray diffraction data and help to fabricate new CeO_2-ZrO_2 catalysts with higher oxygen storage capacity and better redox performance. In this work, the optimal zirconium content x for our $Ce_{1-x}Zr_xO_2$ catalysts was 0.5. In prospect, we believe that the as-presented results on the homogeneous nanostructured $Ce_{1-x}Zr_xO_2$ ($x = 0-0.8$) solid solutions in this paper will bring about both adequate academic and practical interests not only on the research of the synthetic methodology, bulk and surface chemistry, and texture properties of the widely used CeO_2-ZrO_2 mixed oxides, but also on the development of exceptional TWCs with high OSC values and high thermal stability.

Supporting Information Available: Elementary analyses of N, C, H contents and total weight loss in the as-prepared $Ce_{1-x}Zr_xO_2$ samples (Table 1S), summary of the principal XPS binding energies of the as-prepared $Ce_{1-x}Zr_xO_2$ samples (Table 2S), FTIR spectrum of the as-prepared $Ce_{0.5}Zr_{0.5}O_2$ sample (Figure 1S), PXRD patterns and Raman spectra of the $Ce_{1-x}Zr_xO_2$ samples calcined at 1273 K for 4 h (Figure 2S), and $CO-OSC$ values of the $Ce_{1-x}Zr_xO_2$ catalysts as a function of particle sizes and BET specific surface areas (Figure 3S). This material is available free of charge via the Internet at http://pubs.acs.org.

References and Notes

(1) Li, R. X.; Yabe, S.; Yamashita, M.; Momose, S.; Yoshida, S.; Yin, S.; Sato, T. *Solid State Ionics* **2002**, *151*, 235.

(2) Steele B. C. H. *Nature* **1999**, *400*, 619.

(3) Fornasiero, P.; Balducci, G.; Di Monte, R.; Kašpar, J.; Sergo, V.; Gubitosa, G.; Ferrero, A.; Graziani, M. *J. Catal.* **1996**, *164*, 173.

(4) Kašpar, J.; Fornasiero, P.; Graziani, M. *Catal. Today* **1999**, *50*, 285.

(5) Kašpar, J.; Fornasiero, P.; Hickey, N. *Catal. Today* **2003**, *77*, 419.

(6) De Leitenburg, C.; Trovarelli, A.; Zamar, F.; Maschio, S.; Dolcetti, G.; Llorca, J. *J. Chem. Soc., Chem. Commun.* **1995**, 2181.

(7) Hirano, M.; Miwa, T.; Inagaki, M. *J. Solid State Chem.* **2001**, *158*, 112.

(8) Rossignol, S.; Gérard, F.; Duprez, D. *J. Mater. Chem.* **1999**, *9*, 1615.

(9) Alifanti, M.; Baps, B.; Blangenois, N.; Naud, J.; Grange, P.; Delmon, B. *Chem. Mater.* **2003**, *15*, 395.

(10) Cabañas, A.; Darr, J. A.; Lester, E.; Poliakoff, M. *J. Mater. Chem.* **2001**, *11*, 561.

(11) Hirano, M.; Kato, E. *J. Am. Ceram. Soc.* **1999**, *82*, 786.

(12) Pengpanich, S.; Meeyoo, V.; Rirksomboon, T.; Bunyakiat, K. *Appl. Catal. A Gen.* **2002**, *234*, 221.

(13) Kašpar, J.; Fornasiero, P. *J. Solid State Chem.* **2003**, *171*, 19.

(14) Balducci, G.; Kašpar, J.; Fornasiero, P.; Graziani, M.; Islam, M. S.; Gale, J. D. *J. Phys. Chem. B* **1997**, *101*, 1750.

(15) Balducci, G.; Kašpar, J.; Fornasiero, P.; Graziani, M.; Islam, M. S. *J. Phys. Chem. B* **1998**, *102*, 557.

(16) Madier, Y.; Descorme, C.; Le Govic, A.-M.; Duprez, D. *J. Phys. Chem. B* **1999**, *103*, 10999.

(17) Mamontov, E.; Egami, T.; Brezny, R.; Koranne. M.; Tyagi, S. *J. Phys. Chem. B* **2000**, *104*, 11110.

(18) Balducci, G.; Islam, M. S.; Kašpar, J.; Fornasiero, P.; Graziani, M. *Chem. Mater.* **2000**, *12*, 677.

(19) Rodriguez, J. A.; Hanson, J. C.; Kim, J.-Y.; Liu, G.; Iglesias-Juez, A.; Fernández-García, M. *J. Phys. Chem. B* **2003**, *107*, 3535.

(20) Langford, J. I. *J. Appl. Crystallogr.* **1971**, *4*, 259.

(21) Langford, J. I. *J. Appl. Crystallogr.* **1973**, *6*, 190.

(22) Guinier, A. *Theorie et Technique de la Radiocristallographie*, 3rd ed.; Dunod: Paris, France, 1964; p 482.

(23) Dekeijser, T. H.; Langford, J. I.; Mittemeijer, E. J.; Vogels, A. B. P. *J. Appl. Crystallogr.* **1982**, *15*, 308.

(24) Hori, C. E.; Permana, H.; Ng, K. Y. S.; Brenner, A.; More, K.; Rahmoeller, K. M.; Belton, D. *Appl. Catal. B Environ.* **1998**, *16*, 105.

(25) Pfau, A.; Schierbaum, K. D. *Surf. Sci.* **1994**, *321*, 71.

(26) Orel, Z. C.; Orel, B. *Phys. Status Solidi B* **1994**, *186*, K33.

(27) Rao, G. R.; Sahu, H. R. *Proc. Indian Acad. Sci. (Chem. Sci.)* **2001**, *113*, 651.

(28) Yashima, M.; Morimoto, K.; Ishizawa, N.; Yoshimura, M. *J. Am. Ceram. Soc.* **1993**, *76*, 1745.

(29) Yashima, M.; Morimoto, K.; Ishizawa, N.; Yoshimura, M. *J. Am. Ceram. Soc.* **1993**, *76*, 2865.

(30) Yashima, M.; Arashi, H.; Kakihana, M.; Yoshimura, M. *J. Am. Ceram. Soc.* **1994**, *77*, 1067.

(31) Yashima, M.; Ohtake, K.; Kakihana, M.; Yoshimura, M. *J. Am. Ceram. Soc.* **1994**, *77*, 2773.

(32) López, E. F.; Escribano, V. S.; Panizza, M.; Carnasciali, M. M.; Busca, G. *J. Mater. Chem.* **2001**, *11*, 1891.

(33) Kašpar, J.; Di Monte, R.; Fornasiero, P.; Graziani, M.; Bradshaw, H.; Norman, C. *Top. Catal.* **2001**, *16−17*, 83.

(34) Kašpar, J.; Fornasiero, P.; Balducci, G.; Di Monte, R.; Hickey, N.; Sergo, V. *Inorg. Chim. Acta* **2003**, *349*, 217.

(35) Shukla, S.; Seal, S. *J. Phys. Chem. B* **2004**, *108*, 3395.

(36) Garvie, R. C. *J. Phys. Chem.* **1965**, *69*, 1238.

(37) Chatterjee, A.; Pradhan, S. K.; Datta, A.; De, M.; Chakravorty, D. *J. Mater. Res.* **1996**, *9*, 263.

(38) Xu, G.; Zhang, Y. W.; Han, B.; Li, M. J.; Li C.; Yan, C. H. *Phys. Chem. Chem. Phys.* **2003**, *5*, 4008.

(39) Martínez-Arias, A.; Fernández-García, M.; Ballesteros, V.; Salamanca, L. N.; Conesa, J. C.; Otero, C.; Soria, J. *Langmuir* **1999**, *15*, 4796.

(40) Lin, J. D.; Duh, J. G. *J. Am. Ceram. Soc.* **1997**, *80*, 92.

(41) Hirano, M.; Kato, E. *J. Am. Ceram. Soc.* **1996**, *79*, 777.

(42) Muha, G. M.; Vaughan, P. A. *J. Chem. Phys.* **1960**, *33*, 194.

(43) Ramamoorthy, R.; Ramasamy, S.; Sundararaman, D. *J. Mater. Res.* **1999**, *14*, 90

(44) Huang, D. X.; Chen, C. L.; Chen, L.; Jacobson, A. J. *Appl. Phys. Lett.* **2004**, *84*, 708.

(45) Bozo, C.; Guilhaume, N.; Garbowski, E.; Primet, M. *Catal. Today* **2000**, *59*, 33.

(46) Pengpanich, S.; Meeyoo, V.; Rirksomboon, T.; Bunyakiat, K. *Appl. Catal. A Gen.* **2002**, *234*, 221.

(47) Ranga Rao, G.; Kašpar, J.; Meriani, S.; Di Monte, R.; Graziani, M. *Catal. Lett.* **1994**, *24*, 107.

(48) Fornasiero, P.; Di Monte, R.; Ranga Rao, G.; Kašpar, J.; Meriani, S.; Trovarelli, A.; Graziani, M. *J. Catal.* **1994**, *151*, 168.